Cold Regions Science and Technology 237 (2025) 104534

Contents lists available at ScienceDirect

Cold Regions Science and Technology

journal homepage: www.elsevier.com/locate/coldregions

Investigating emerging boulder impacts on snowpack ablation

Eole Valence [a,*], Bastien Charonnat [b], Michel Baraër [b], Kaiyuan Wang [c], Jeffrey M. McKenzie [a]

[a] Department of Earth and Planetary Sciences, McGill University, Montreal H3A 0E8, Canada
[b] Hydrology, Climate and Climate Change (HC3) Laboratory, Ecole de Technologie Superieure, Montreal H3C 1K3, Canada
[c] Department of Earth, Environmental & Planetary Sciences, Brown University, Providence, RI, United States

ARTICLE INFO

Keywords:
Snowpack
Snow monitoring
LiDAR
Thermal infrared
Photogrammetry

ABSTRACT

The impact of emergent boulders within a thinning and melting snowpack remains poorly understood. Our research examines how boulders, exposed by melting snowpack influence the spatial and temporal patterns of snow ablation in the Shár Shaw Tagà Valley, Yukon, Canada. A multimethod approach, combining thermal infrared time-lapse imaging, drone-based photogrammetry, and terrestrial laser scanning, was used to monitor snow surface temperature, elevation changes, and melt variability. This approach underscores the importance of comprehensive techniques in assessing the spatial and temporal variability of snow surface temperature and topography. Results indicate that boulders accelerate snowmelt in their vicinity during the ablation season, with snow surface thermal characteristics shaped by local terrain and meteorological conditions. The fastest rates of ablation occur during periods of mild weather with no precipitation. These findings highlight the role of boulders as micro-scale heat sources that can modify energy fluxes and influence broader melt patterns in subarctic alpine environments. Understanding these processes is essential for improving snowmelt modelling and predicting hydrological changes in mountain regions affected by climate change.

1. Introduction

Recent observations indicate a widespread decrease in snow cover extent and duration globally (Notarnicola, 2022). Climate change is expected to further transform snowpacks, leading to a further reduction in seasonal snowpack depth (Dierauer et al., 2021), including a decline in winter maximum snow water equivalent (Sun et al., 2019), and an earlier onset of spring melt (Gergely et al., 2010). Additionally, given that the Arctic is warming faster than the global average (Rantanen et al., 2022) and that rate of warming is amplified with elevation (Mountain Research Initiative EDW Working Group, 2015), drastic changes in snow conditions are anticipated in northern mountainous regions.

With climate change, understanding the behaviour and characteristics of snowpack formation and melting in mountain environments is essential for predicting hydrologic functionality. Among studies that have focused on the physical properties of snowpacks (e.g. Kinar and Pomeroy, 2015; Mellor, 1977; Pomeroy and Brun, 2001), many have approached snowpack hydrological behaviour through one-dimensional energy and mass budgets (Bartelt and Lehning, 2002; Brun et al., 1989; Jordan, 1991; Mas et al., 2018; Rutter et al., 2008; Turcotte et al., 2007), making it difficult to capture the impact of snowpack spatial heterogeneity on catchment hydrology (Paquotte and Baraer, 2022). This is particularly true in mountain environments, where the physical characteristics of the snowpacks are highly heterogeneous (Wetlaufer et al., 2016).

The spatial heterogeneity of snow cover characteristics is not the only factor driving the variability in meltwater contribution to catchment hydrology. Melt patterns are influenced by surrounding terrain features such as trees, rock debris, and topography, all of which modify local energy and mass budgets. For example, it has been shown that snowmelt is enhanced near tree trunks in subarctic environments due to longwave radiation (Woo and Giesbrecht, 2000). Longwave emissions from surrounding terrain have also been shown to be responsible for snow and ice melt in mountainous environments too (e.g., Aubry-Wake et al., 2018; Robledano et al., 2022). Increased melting of heterogeneous or patchy snow cover, driven by advective fluxes from bare patches of ground, has also been reported (Marsh and Pomeroy, 1996). Therefore, it is anticipated that boulders emerging from a thinning snowpack will affect the surrounding snow melting rate (Grünewald et al., 2010). The presence of boulders may modify the sensible heat fluxes originating from the snow-free area to the snowpack (Mott et al., 2011) and they

* Corresponding author.
E-mail address: eole.valence@mail.mcgill.ca (E. Valence).

https://doi.org/10.1016/j.coldregions.2025.104534
Received 24 February 2025; Received in revised form 17 April 2025; Accepted 26 April 2025
Available online 28 April 2025

may also alter the radiative budget of the snowpack (Markstrom et al., 2011). The energy provided by a boulder via conduction to the surrounding snow may also affect the adjacent snowpack while the boulder and snow are in contact (Gray et al., 1995). However, the boulders influence on the surface energy balance and melt patterns, as well as the extent of this phenomenon are still poorly understood.

The objective of our study is to combine ground-based thermal infrared observations, terrestrial laser scanning, and periodic drone-based snow cover topography measurements to investigate to what extent and in what manner does an emerging rock boulder influence the ablation of a subarctic snowpack.

2. Study site and meteorological conditions

The study area is a sub-catchment of the Shár Shaw Tagà Valley in southwestern Yukon, Canada. This subarctic alpine valley is located within the Kluane First Nation and White River First Nation territory, in the Kluane National Park and Reserve. Shár Shaw Tagà has been referred to by its non-indigenous toponym, "Grizzly Creek", in previous studies (Evin et al., 1997; Johnson, 1978; Tjoelker et al., 2024). The sub-catchment covers 6 km^2 (Fig. 1), with an elevation range from approximately 1500 to 2600 m above mean sea level (m.a.s.l.). The focus area is a 1000 m^2 region located at 61.083116°N, 139.12816°W at an elevation of 1835 m.a.s.l. (Fig. 1). The site is on a rock glacier where a substantial number of boulders emerge from the snow cover in spring. At the start of the measurement period, on June 12, 2022, approximately 70 % of the focus area was covered by snow. The snow coverage decreased to less than 20 % by the end of the study on June 20, 2022. A 6 m^3 boulder that emerged partially from the snow at the beginning of the study was chosen as the focus for our investigation. This boulder is located at the edge of a 10 m long East-facing scree slope of approximately 30°, on a rock glacier lobe.

An automatic weather station (AWS) is located at approximately 2100 m a.s.l. and records air temperature, precipitation, and shortwave radiation, at 15-min intervals (Supplemental Table 1) with a Campbell Scientific CR300 data logger.

Observations were made between June 12 and June 20, 2022. Over this period, the hourly air temperature ranged from −1.0 °C to +10 °C, and the site received a total of 47 mm of precipitation at the AWS location (Fig. 2). Most of the precipitation was rain, with a few short episodes of wet snow. Based on these observations, the study period is divided into three meteorological episodes: i) the 'Wet First Period' (W.1.P.; June 12 at 00:00 to June 16 at 00:00) which was mainly overcast, with 30 mm of precipitation. During this episode, air temperature ranged from −1.0 °C to +6 °C. The daily average incoming shortwave radiation during this episode reached 184 W/m^2 on June 15. ii) The 'Mild Second Period' (M.2.P.; June 16 at 00:00 to June 19 at 00:00) characterized by clear sky conditions. Air temperatures ranged from +1 °C to +10 °C with a strong diurnal pattern. Clear skies allowed daily average shortwave incoming radiation to reach 324 W/m^2 on June 18 and there was no measured precipitation. iii) The 'Wet Third Period' (W.3.P.; June 19 at 00:00 to June 20 at 16:00) was overcast with 17 mm of liquid precipitation. Air temperatures ranged from 0 °C to +8 °C, and the daily average shortwave radiation decreased to 155 W/m^2.

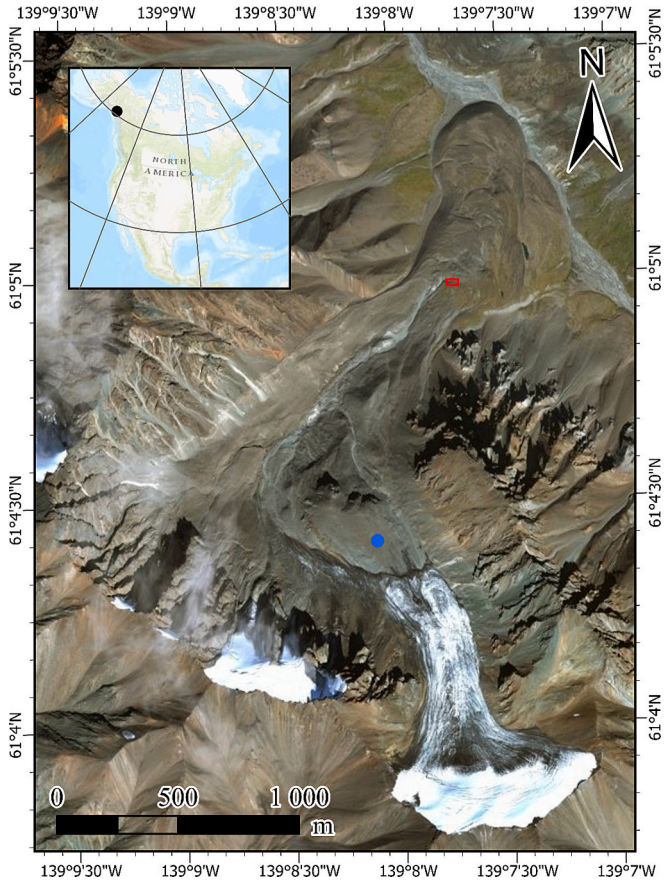

Fig. 1. Field site in the sub-catchment of Shár Shaw Tagà. The solid blue circle indicates the location of the automatic weather station location. The study area is represented by a red rectangle. Basemap credits: Esri, Maxar, Earthstar Geographics, National Geographic, and the GIS User Community. (For interpretation of the references to colour in this figure legend, the reader is referred to the web version of this article.)

3. Methods

3.1. Method overview

This study presents observations of snow surface topography changes measured by terrestrial laser scanner monitoring and repetitive photogrammetry surveys, and monitoring of snow and adjacent rock boulder skin temperature using a thermal infrared camera. The observations are

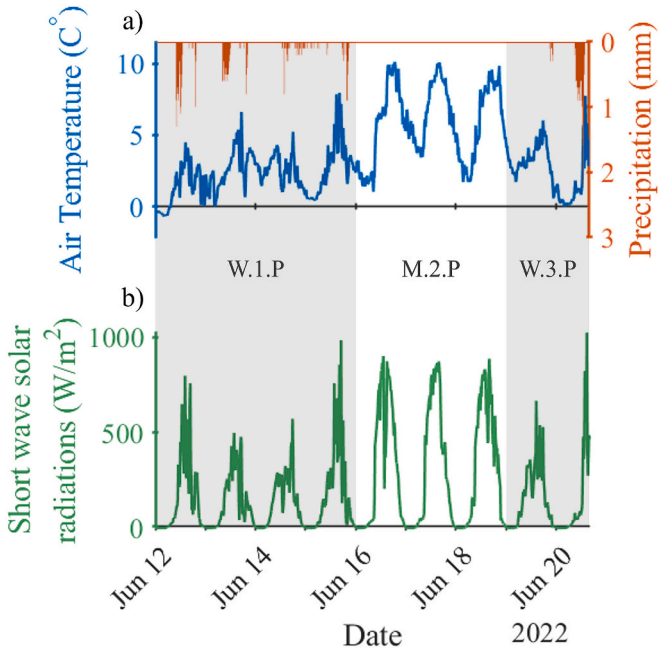

Fig. 2. a) Air temperatures (in blue) and Precipitation (in orange); b) Short wave solar radiations (in green) at the automatic weather station. Semi-transparent grey shadings represent the 'Wet First Period' and 'Wet Third Period'. (For interpretation of the references to colour in this figure legend, the reader is referred to the web version of this article.)

then compared to a model of longwave emitted by the adjacent rock boulder to the snow. The terrestrial laser scanner and the thermal camera were placed in a snow-free zone of the area at 8 m above the snow surface and 40 m away from the studied boulder, allowing for an angle of view perpendicular to the snow surface for both devices. Daily drone-based photogrammetry flights measured snow topographical changes around the boulder. Ground control points were installed in snow-free areas on and around the boulder to calibrate and validate the observational results. The control points locations were chosen to cover the survey area homogeneously including different slope aspects, without disrupting the snow cover within the ROIs. Additional details, such as the number of control points used and their accuracy are described below. Finally, snow pits were dug following the method presented in Valence et al. (2022) at the beginning and the end of the survey to measure the snow density and approximate liquid water content (see Supplemental Fig. S1 for snow pits and ground control points localizations).

We selected three Regions of Interest (ROIs) to analyze the results: (i) Rock ROI, characterizing the south side of the boulder; (ii) Snow Close ROI, consisting of snow adjacent to and potentially affected by the Rock ROI; and (iii) Snow Reference ROI, a reference region of snow 3 m away from the boulder, and assumed to be outside the influence area of the boulder (Fig. 3). Finaly, we selected a 3 m long profile perpendicular to the Rock ROI – Snow Close ROI interface to perform a 2D analysis of the Rock ROI longwave emission to the adjacent snow.

The Rock ROI is a rectangular area measuring 1.7 × 0.9 m^2 on the surface of the boulder, which was partially exposed at the beginning of the survey. At the beginning of the study, this ROI covered the area

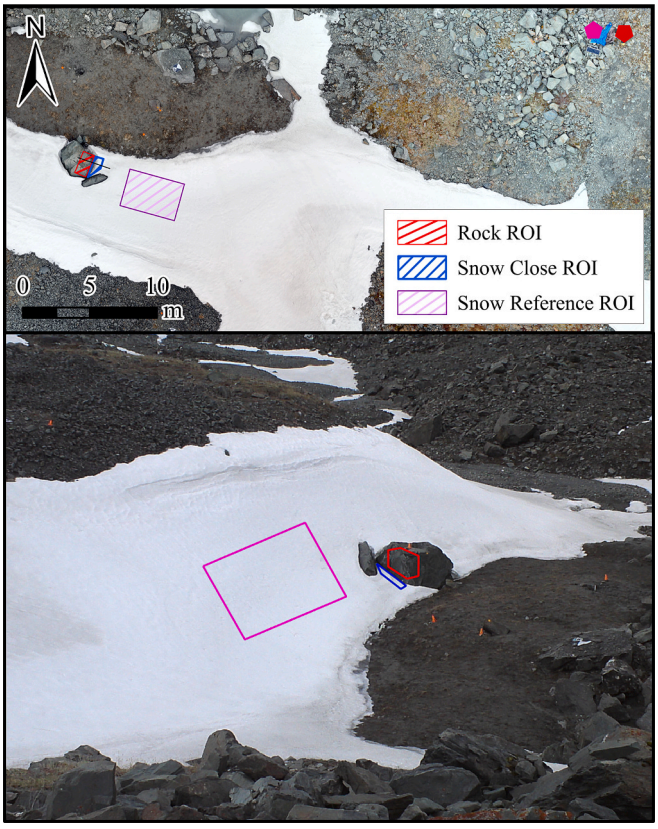

Fig. 3. The first panel shows an orthophoto of the snowpack area produced using drone photogrammetry (June 20, 2022); while the second panel is a picture of the snowpack area taken from the TIR camera point of view (June 20, 2022). The Lidar sensor and the thermal camera are indicated by a red and pink pentagon, respectively; and the 2D profile used for modelling is display as a black line. (For interpretation of the references to colour in this figure legend, the reader is referred to the web version of this article.)

overlapping between the LiDAR cloud point, the thermal infrared camera image and the photogrammetry result. The Snow Close ROI covers 0.8 m^2 South-East oriented snow area with a constant slope of approximately 30° at the end of the survey. The boundaries of the Snow Close ROI were chosen as a rectangle with the width of 1.7 m, the same width as the Rock ROI and with a length of 70 cm. The ROI boundaries are clipped to contain only areas closer to the Rock ROI than to any other snow-free surfaces by the end of the measurement period and that are within the fields of view of both observation devices. The Snow Reference ROI is the largest snow area with the same slope and with the same orientation as the Snow Close ROI. This ROI is at minimum 1 m away from any snow free surface obstacle at the end of the survey. The snow cover on both Snow ROIs lies over a scree of rock debris of smaller size but similar to the boulder of Rock ROI.

The evolution of the snow surface topography was monitored using LiDAR observations to compare snow surface elevation changes rates between the Snow Close ROI and the Snow Reference ROI. Photogrammetry provided a more detailed representation of the snow topography near the boulder. By integrating photogrammetry with time-lapse thermal imagery, a 2D model of the boulder's longwave emissions and their impact on snow ablation was developed for the three meteorological periods.

3.2. LiDAR observations

LiDAR point clouds were obtained using a Blickfeld Cube 1 LiDAR sensor, with a laser wavelength of 905 nm. The Cube 1 has a field of view of 70° × 30°, collecting 400 lines with 400 points per line for each frame, resulting in approximately 130 points per m^2. The device was mounted on a 3-m-high mast and controlled by a Raspberry Pi 4B to automatically turn on and record frames every hour from June 12 at 00:00 to June 20 at 16:00. The LiDAR station was 40 m away and 11 m higher than the ROIs. Five reflective targets were installed on snow-free rocks, perpendicular to the LiDAR beams and geolocated with a Topcon DGPS with an accuracy of ±0.3 cm.

LiDAR data were processed using a Python v3.9 script to automate steps in CloudCompare v2.13, including importing data, applying a noise filter, translating and rotating to georeference the point cloud with the LiDAR targets, computing the cloud-to-cloud distance (C2C; i.e., the distance of every point in a cloud point with respect to the closest one in the second cloud point). The vertical distance (C2C-Z) was computed using the last measurement as reference and extracting results for each ROI for each measurement. The mean C2C-Z distance and standard deviation of the two snow ROIs were computed for each measurement to track snow elevation changes over time. The LiDAR orientation was adjusted on June 14 at approximately 12:30, after two and a half days of measurement, as only three reflective targets were initially detectable in the LiDAR point clouds. To estimate alignment error, the absolute C2C distance for the Rock ROI was computed, comparing each measurement to the last recorded measurement.

Trends in ROI snow median surface elevation changes were assessed for each meteorological period considered. Trends were calculated using three nonparametric tests: the Mann-Kendall test, modified Mann-Kendall test, and Spearman's rank correlation (rho), with a 0.05 significance level to reject the null hypothesis (Chesnokova et al., 2020). The Mann-Kendall test detects monotonic trends by comparing each observation with earlier ones, though positive serial correlation can inflate Type I errors (Bevan and Kendall, 1971). The modified Mann-Kendall test addresses this by adjusting variance with autocorrelation coefficients (Hamed, 2009). To avoid miscalculation induced by the Lidar adjustment or due to diurnal bias in measurement, only continuous periods of multiple full consecutives days where considered. Therefore, trends were computed from June 12 at 12:00 to June 14 at 12:00 for W.1.P (2 days); from June 16 at 00:00 to June 19 at 00:00 for M.2.P (3 days); and from June 18 at 16:00 to June 20 at 16:00 for W.3.P (2 days). The trend calculation of W.3.P starts before the beginning of

the last period: when the mean surface elevation difference to the last measurement of one of the two snow ROI reaches 0. Spearman's rho evaluates rank correlations but is sensitive to outliers (Croux and Dehon, 2010). Trend magnitudes were calculated for each of the three periods, using the Theil-Sen estimator, which computes the median slope between observation pairs (Sen, 1968).

3.3. Photogrammetry measurements

A DJI Mavic 2 Pro drone was used for nine flights over the study area to acquire RGB images for photogrammetry. During each flight, each lasting approximately 25 min, the drone captured around 300 images. The drone flew at a target elevation of 20 m above the landing area, situated close to the LiDAR and TIR sensors. The images, collected with 80 % overlap, were processed using Pix4Dmapper software to produce digital surface models (DSM) and point clouds. The horizontal resolution of the resulting DSM is 0.4 cm per pixel. The vertical accuracies of the final point clouds, ranging from 5 to 10 cm, were enhanced using ground control points (GCPs). For each survey, seven GCPs were established on snow-free ground near the study area (see Supplemental Fig. S1) following Shu et al. (2023). These GCPs were geolocated using a Topcon DGPS with real-time kinematic (RTK) correction, achieving an accuracy of ±0.3 cm. Cloud alignment was assessed using CloudCompare v2.13, comparing the Rock ROI's position across flights, with the last flight on June 20 as the reference. Following Clemens-Sewall et al. (2024), a Bayesian statistical model was used to compare the histogram of the C2C distance changes of the Rock ROI, which remained immobile during data collection.

Vertical changes in snow depth were computed using the vertical Cloud-to-Cloud (C2C-Z) distance calculation tool, referencing the last photogrammetry cloud point on June 20. The results for the two snow ROIs were used to compute the mean and standard deviation of snow surface elevation differences.

As the snow melted, a trench or gap formed between the boulder and the snowpack. To capture the trench width over time between the Snow Close ROI and the Rock ROI, lateral changes in cloud points were computed using the Cloud-to-Cloud distance calculation tool on two orthogonal horizontal axes (C2C-X and C2C—Y). The surface used for calculating trench enlargement was fixed daily to capture the lateral ablation of the snowpack.

For each day, a 3 m long profile was extracted from the photogrammetry cloud points, and this profile is used for the long wave radiation model presented in Section 3.4.

3.4. Thermal infrared monitoring

Thermal infrared images were taken at 15-min intervals from June 14, 2022, at 16:00 to June 20, 2022, at 16:00. The TIR camera was positioned next to the Lidar instrument at an elevation 9 m higher than the ROIs (Fig. 3). We used a Jenoptik VarioCam HD with a resolution of 1024 × 768 pixels. The camera features an uncooled microbolometer and operates within the thermal infrared wavelength range of 7.5–14 μm, with a manufacturer-stated accuracy of ±1.5 °C. Therefore, the Rock ROI, Snow Close ROI and Snow Reference ROI represent 1795, 433 and 23,124 pixels, respectively. Following the method by Aubry-Wake et al. (2018), we installed five temperature control points (CPs) near the snowpack margin; the characteristics of the temperature CP sensors are presented in Supplemental Table 1. The sensors were placed under small piles of rocks to ensure thermal contact with the ground and to avoid direct solar radiation. As the sensors were at ground level, their measured temperature is considered the 'true' shaded surface temperature.

The TIR images were processed to obtain calibrated surface-temperature data following Aubry-Wake et al. (2015), which uses Planck's law to convert radiance measured by the TIR to surface temperature and adjusts temperatures with an offset correction based on the mean temperature from three of the five sensors (Baker et al., 2019). The Hobo temperature sensors recorded data at 1-h intervals, so the corrected temperatures obtained with the TIR are also at 1-h intervals.

The average corrected temperature of each ROI is used as input for a simple 2D longwave model following the methodology presented by Woo and Giesbrecht (2000). The average long wave radiation emitted by the Rock ROI surface (L_{rock}), by the surface of the Snow Close ROI (L_{snow_close}), and the Snow Reference ROI ($L_{snow\_reference}$) are computed for each meteorological periods (W.1.P., M.2.P. or W.3.P.) using the Planck's law:

$$L = \varepsilon.\sigma.T^4, \tag{1}$$

where L represent the average long wave radiation emitted in $W.m^{-2}$ for the considered meteorological period; ε the surface emissivity for the boulder and the snow, set as 0.9 and 0.99, respectively; σ the Stephan Boltzmann constant ($5.67.10^{-8}$ $W.m^{-2}.K^{-4}$), and T (in K) is the mean corrected ROI temperature value over the considered meteorological period.

The net long wave radiation (L^*) in $W.m^{-2}$ is then computed as:

$$L^* = H \Big/ H_t.L_{rock} - \left(L_{snow_{close}} - L_{snow_{reference}}\right) \tag{2}$$

where H is the hypothetical hemispherical area emitting longwave radiation to a point on the snow surface, located at a distance x from the boulder in m; H_t is the surface area of the hypothetical hemisphere which receives longwave radiation from the boulder. The ratio H/H_t is adapted from Woo and Giesbrecht (2000):

$$\frac{H_t}{H} = \arctan\left(\frac{l}{2.x}\right).\sin^2\left(arctan\left(\frac{h - S_i}{x}\right)\right) \Big/ \pi \tag{3}$$

with l the boulder width in m, h the boulder height in m and S_i the snow height at the beginning of the considered meteorological period in m at a distance x before ablation. The snow height is extracted from the photogrammetry results.

The snowpack was considered as mature during the period of study as the snow at the snow pits location had a temperature of 0 °C allowing all of the received energy to be used for melting. Therefore, the snow loss during the considered meteorological period at a distance x from the boulder ($\Delta s(x)$ in m) can be express as:

$$\Delta s(x) = \frac{L_*}{L_f \cdot \rho_{snow}} \tag{4}$$

where $L_f$is the snow specific latent heat of fusion set as 333 kJ/kg and ρ_{snow} is the average snow relative density measured by snow pits at the beginning and end of the study period (0.3).

To compare the observed snow ablation with the computed one, it is required to add to the snow loss expected if there was no emerging boulder: being the mean value of the vertical snow height changes measured on Snow Reference ROI by photogrammetry, assumed to be equal to the ablation.

4. Results

4.1. Snow surface vertical changes

Fig. 4 presents the surface elevation changes of each ROI over time from both the photogrammetry and terrestrial LASER scanning (TLS) surveys.

Fig. 4a illustrates the evolution of the mean surface elevation of the Rock ROI as measured by photogrammetry and TLS. A 2–3 cm shift was observed between the values of June 14 at 12:00 and 13:00 in the TLS data corresponding to a LiDAR position adjustment. This shift was corrected by applying an offset to all elevation difference values recorded prior to June 14 at 12:00. Several smaller and temporally inconsistent

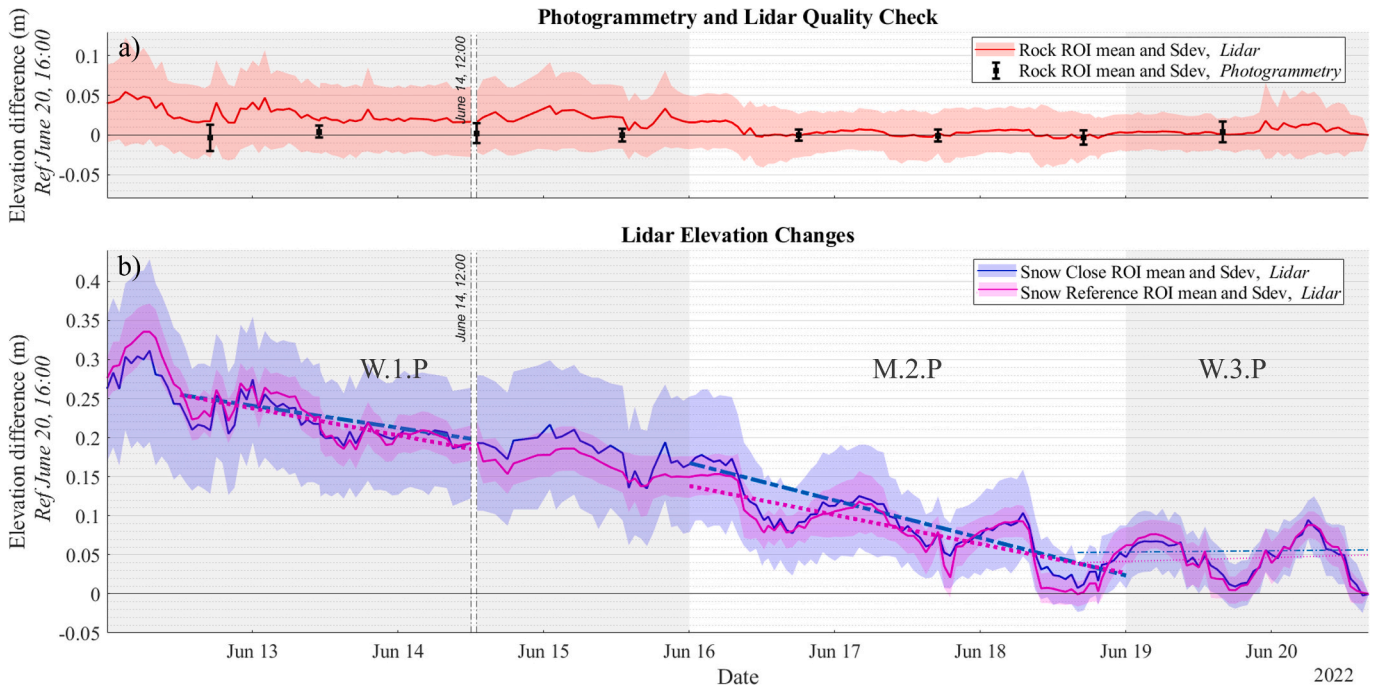

Fig. 4. a) Rock ROIs surface elevation changes estimated from photogrammetry (squares) and TLS (line); b) snow ROIs elevation changes from TLS. All elevations are expressed as the difference with the last measurement. Dotted pink and dashed blue lines show slopes in elevation measurements. Trends being statistically significant ($\alpha < 0.05$) for each of the three tests are displayed in bold. Pastel colour surfaces represent plus and minus one standard deviation for the TLS measurements. Semi-transparent grey shadings represent the 'Wet First Period' and 'Wet Third Period'. The dashed vertical line marks the moment when the TLS orientation was adjusted. (For interpretation of the references to colour in this figure legend, the reader is referred to the web version of this article.)

shifts in mean elevation change are also observed in the LiDAR dataset. We hypothesize that these shifts may be due to poor-quality point cloud data or an insufficient number of points. Excluding this deviation, both methods align closely with zero, validating their accuracy since the boulder was stationary throughout the measurement period. However, the average standard deviation for TLS (3.6 cm) is over twice that of photogrammetry (1.0 cm).

The TLS data show greater variability due to two factors: i) there are fewer data points in TLS (600) compared to photogrammetry (24,000), limiting statistical robustness, and ii) the TLS data are not as well aligned as the photogrammetry data. Beyond the position adjustment on June 14, no trends or biases were evident in TLS data. Standard deviation integrates elevation differences and measurement noise. For the fixed Rock ROI, photogrammetry's precision reflects minimal misalignment error. In contrast, TLS precision is affected by insufficient data points for unbiased distributions, and beam diffraction from the angle between the LiDAR view and the surface. A more optimized experimental setup might reduce, though not eliminate, these uncertainties.

Fig. 4b presents the surface elevation changes of the snow ROIs over the study period, revealing a diurnal fluctuation in the elevation difference measured using TLS. This diurnal pattern is particularly pronounced from the end of the 'Wet First Period'. The influence of snow characteristics such as grain shape and size, density, and liquid water content on its optical properties in the NIR spectrum is well-documented (e.g., Hannula and Pulliainen, 2019; Warren, 2019). The pronounced diurnal oscillation pattern in the elevation measurements during clear sky periods suggests that the surface conditions of the snow might have affected the distances measured by the TLS.

Regression lines in Fig. 4b are presented for the TLS measurements. A general agreement between the two snow ROIs is observed, with more pronounced ablation and/or snow compaction occurring during the 'Mild Second Period' compared to the other two periods. There appears to be a difference in slopes between the Snow Close ROI and the Snow Reference ROI. The differences in regression curves indicate that the ablation and/or snow compaction is greater at the Snow Reference ROI during the 'Wet First Period', is greater at the Snow Close ROI during the 'Mild Second Period', and is of comparable rates between both ROIs during the final 'Wet Third Period'.

Table 1 presents the results of statistical trend tests, confirming slope evolution across the three study periods for the two snow ROIs. The exception is for the Snow Reference ROI during the 'Wet Third Period,' where the calculated slope is not statistically significant. Trend analysis also shows disparities in snow surface topography changes for the three studied periods. During the 'Wet First Period', both the Snow Close ROI and the Snow Reference ROI showed an average elevation decrease of approximately 3 cm per day, with a slightly steeper trend slope for the Snow Reference ROI. During the 'Mild Second Period', both Snow Close ROI and Snow Reference ROI median surface elevations significantly decreased by 5 and 4 cm per day, respectively, suggesting that the area close to the boulder was melting or settling faster than the area further away from the boulder's influence. Finally, no measurable trend was shown to be significant during the 'Wet Third Period'.

During the 'Wet First Period', TLS surface elevation changes exhibit higher variability in the Snow Close ROI than in the Snow Reference ROI. This result highlights that as the boulder is uncovered by snow, it affects the snow heterogeneously within the Snow Close ROI. The heterogeneity within the Snow Close ROI decreases progressively during the 'Mild Second Period' and matches the Snow Reference ROI by the end of the measurement period ('Wet Third Period'). These observations suggest that the topography of parts of the Snow Close ROI changed differently than the Reference ROI during the 'Mild Second Period', with the Rock ROI amplifying the melting of parts of the Snow Close ROI due to the warm and sunny weather.

Interestingly, TLS data for both snow ROIs follow a diurnal pattern, with higher apparent surface elevations during the night and lower during the afternoon. The relative increase in snow elevation during night is larger during and after the 'Mild Second Period' of data collection (Fig. 4b). While the mean elevation difference between nights and days increased up to 4 cm during the 'Wet First Period', it increased up to 9 cm during the 'Mild Second Period' and during the 'Wet Third

Table 1
Results of the trend analysis of the mean elevation difference observed by LiDAR measurement. *p*-values under 0.05 are indicative of a statistically representative trend for the studied period. The Slope of this trend is estimated using the Sen's slope. Trends whose p-values are below 0.05 for the three tests are highlighted in bold.

	Method	Snow Close ROI			Snow Reference ROI		
		1st period	2nd period	3rd period	1st period	2nd period	3rd period
p value	Mann-Kendall	1.51 E-5	< 1 E-10	0.770	4.50 E-7	< 1 E-10	0.493
	Mann-Kendall modified	1.51 E-5	< 1 E-10	0.770	4.50 E-7	3.17 E-8	0.493
	Spearman Rho	5.25 E-7	< 1 E-10	0.776	4.05 E-7	< 1 E-10	0.599
Slope (m/d)	Sen's slope	**−0.03**	**−0.05**	+0.00	**−0.03**	**−0.04**	+0.00

Period', exceeding the measurement standard deviations. These patterns are further examined in the Technical Challenges Section.

The results confirm the influence of meteorological conditions on ablation and/or snow compaction rates. However, the heterogeneity within each ROI does not allow for the identification of a distance from the boulder dependent ablation rate measurement. This would explain why the difference in ablation rates between the two snow ROIs appears too limited to draw clear conclusions regarding the boulder's influence.

4.2. Ablation trench formation

Due to the fixed position of the TLS during the measurement period, its viewing angle was not optimal for observing snow ablation processes at the edge of the Rock ROI. However, placing the LiDAR setup very close to the snow near the boulder would disrupt heat exchanges between the boulder and the snow. The following section examines the geometric details provided by photogrammetry.

Figs. 5a-d presents the snow surface elevation changes during the observation period, focusing on the snow cover adjacent to the boulder in the southeast direction. The point clouds as well as the extracted profile are presented for the beginning and end of each meteorological period, on June 12, June 16, June 18 and June 20. These figures show a clear evolution of the snow surface profile in the direct vicinity of the boulder. At the start of the study period, the snow was in contact with the boulder. However, during the study period, a trench formed between the snow and the boulder. Surprisingly, the trench enlarged during the study period, suggesting this process could not be only due to vertical ablation or settlement of the snow. On the first day of measurement, the snow is in contact with the boulder at its base. During the 'Mild Second Period', photogrammetry results reveal enhanced ablation down to the bare ground, resulting in a trench forming between the boulder and the snow. The snow surface slope decreases to almost vertical over this

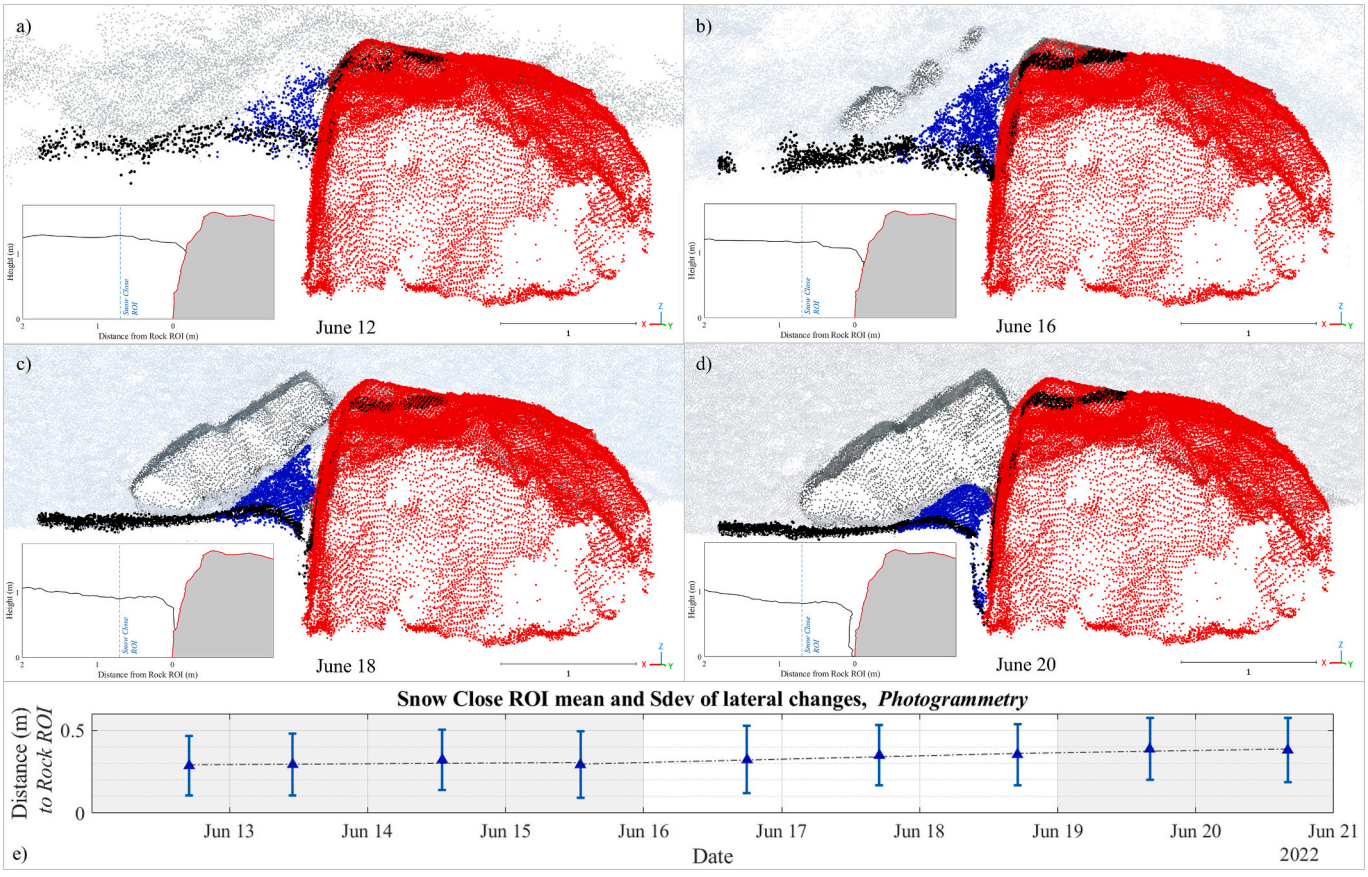

Fig. 5. a) to d) Photogrammetry results focused on the Rock, Snow Close and Receding ROIs at the beginning and end of each meteorological periods, respectively June 12, 16, 18 and 20 (2022). The boulder measurement points are displayed in red, the Snow Close ROI in blue and the extracted profile in black. The cartouches display the interpolated extracted profiles for each date. e) Snow Close ROI lateral distance to the Rock ROI measured with photogrammetry. Triangles indicate the mean values, and the error bars +/− 1 standard deviation for each photogrammetry survey. Semi-transparent grey shadings represent the 'Wet First Period' and 'Wet Third Period'. Linear regressions for the two periods have been displayed with a dashed line. (For interpretation of the references to colour in this figure legend, the reader is referred to the web version of this article.)

period. The trench then opens with a nearly homogeneous horizontal displacement of the trench snow wall.

Fig. 5e shows the horizontal distance between the snow and the boulder, computed from photogrammetry results along two orthogonal horizontal axes (x and y) for each measurement day. This measured distance includes both the projected vertical ablation and settlement increase in the vicinity of the boulder and the trench enlargement due to the boulder. During the 'Wet First Period', the median lateral distance between the snow and the boulder remained constant, with a value of 29 cm, showing no enlargement rate of the trench during the first four days. Conversely, during the 'Mild Second Period', there was a general increase in the median lateral distance, reaching 35 cm on June 18, which may correspond to an enlargement rate of the trench on the order of magnitude of 6 cm in three days. The median lateral distance measured was 38 cm after the final day of the 'Wet third Period', showing an enlargement rate of the trench in the order of magnitude of 3 cm in three days, twice lower than during the 'Mild Second Period'.

The increase of the distance between the snow front and the boulder highlights the enhancement of snow ablation in the vicinity of the boulder, amplified during the clear sky 'Mild Second Period'. The snow ablation amplification appears to continue during the 'Wet Third Period', suggesting the shift between the first and second periods triggered this phenomenon, and the second meteorological shift reduced its impact.

4.3. Snow surface temperature

Fig. 6 presents the corrected TIR temperatures for the ROIs during the study period. The mean ROI temperature represents the average temperature of all pixels within the ROI, the range is the difference between the maximum and minimum temperature of the individual pixels. Note that 'thermal infrared' measures the skin temperature of an object's surface, which may differ from the actual internal temperature of the object. Therefore, it is possible to observe positive TIR snow surface temperatures while the interior of the snowpack remains below 0 °C.

During the 'Wet First Period', the sky was generally cloudy with several precipitation events, and air temperatures ranged from −1 °C to +6 °C (Fig. 2). The mean temperatures of the Rock ROI exhibit a moderate diurnal pattern, increasing from approximately +2 °C at 5:00 AM to +14 °C, +11 °C, and + 7 °C at 16:00 on June 12, 13, and 14, respectively (Fig. 6). The temperature range across the Rock ROI is generally limited, except during the middle of the day when maximum and minimum temperatures differ by 2 °C. Conversely, the temperatures of the two snow ROIs are homogeneous and do not show a clear pattern during the day. For the first three days, mean temperatures measured for both snow ROIs are similar, oscillating around the melting point by ±2 °C during the day.

During the 'Mild Second Period', the weather was sunny with no precipitation events. This period showed a significant change in air temperature patterns with pronounced diurnal variations oscillating between +1 °C and + 10 °C (Fig. 2). The Rock ROI temperatures mirrored these diurnal variations, maintaining stable and homogeneous low temperatures at night and higher temperatures in the afternoons (Fig. 6). The mean surface temperature of the Rock ROI at night stayed below +10 °C, reaching a minimum around 6:00 AM, before sunrise. In the afternoons, temperatures ranged from +13 °C to +30 °C and peaked around 1:00 PM. During this period, the estimated surface temperatures of the two snow ROIs also exhibited a diurnal pattern but with a limited amplitude, ranging from −2 °C at the end of the night to +4 °C in the afternoon. The temperatures across the entire Snow Close ROI gradually became slightly higher than those of the Snow Reference ROI (Fig. 6).

At the end of the study, during the 'Wet Third Period', the mean surface temperature of the Snow Close ROI was 1 °C higher than that of the Snow Reference ROI. Additionally, there was a substantial increase in the range of surface temperatures observed over the Snow Close ROI but not on the Snow Reference ROI surface. The largest temperature range within the Snow Close ROI surface was 1.6 °C, while the largest range for the Snow Reference ROI was 0.3 °C. The Rock ROI temperatures followed a similar diurnal pattern than during the 'Wet First Period', increasing to approximately +14 °C on June 19 at 11:00 PM and decreasing to +3 °C during the night of June 20 at 06:00 AM.

TIR images collected at high frequency demonstrate that short-wave radiation can raise the boulder's surface temperature up to 20 °C higher

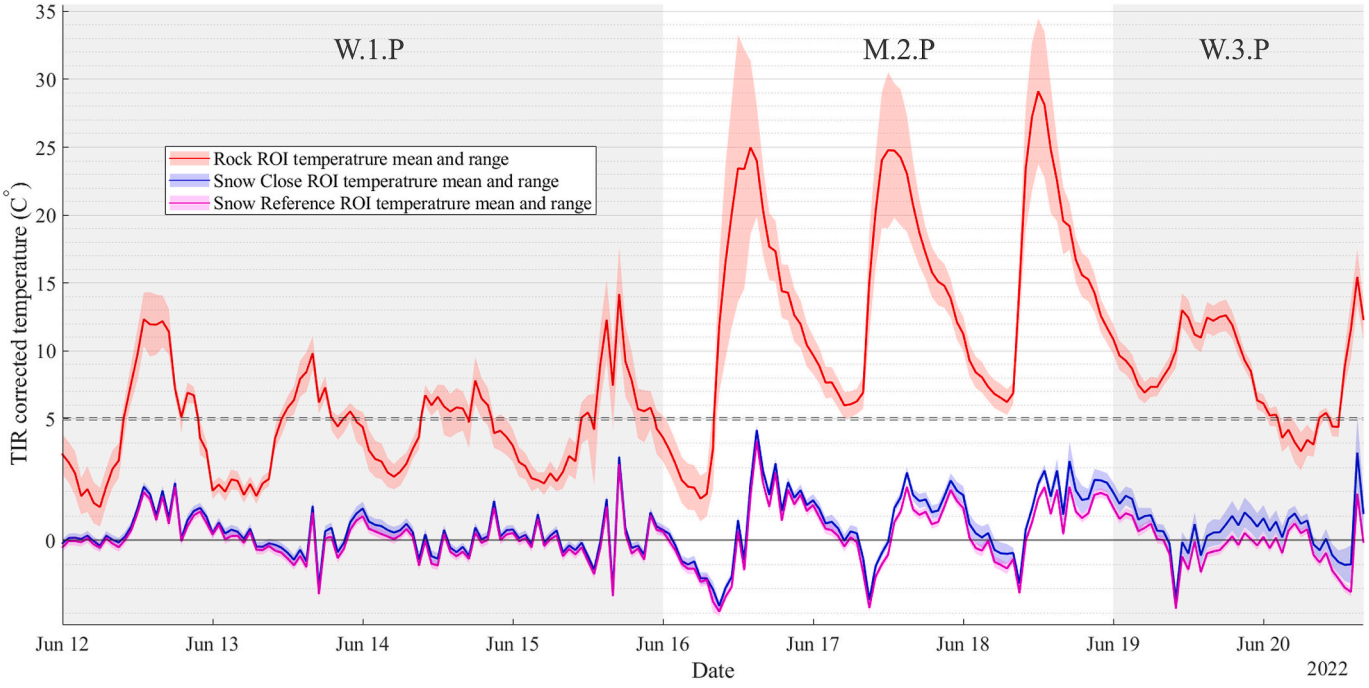

Fig. 6. Corrected surface temperatures from the TIR monitoring of the three ROIs. Semi-transparent grey shadings represent the 'Wet First Period' and 'Wet Third Period'. Note the two horizontal dashed lines mark a change in temperature scale.

than the ambient air temperature on mild, clear days. The same images show that the surface of the snow that is in direct contact with the boulder becomes gradually warmer than the snow surface further away. During the 'Wet First Period', the temperatures of all three ROIs were colder, less variable, and more homogeneous compared to during the 'Mild Second Period' (Fig. 6). Additionally, during the 'Mild Second Period', characterized by higher air temperature and less cloud coverage, the temperature of the Snow Close ROI starts to differentiate from that of the Snow Reference ROI, with higher temperatures and increasing heterogeneity.

The increasing temperature gradient between the Snow Reference ROI and the Snow Close ROI during the 'Mild Second Period' indicates that additional energy is being received in this area. This gradient persists during the 'Wet Third Period', suggesting that heat transfer between the boulder and the surrounding snow continues even when atmospheric heat transfer to the boulder is limited. The accumulation of heat in the rock mass during the 'Mild Second Period' and its subsequent release could explain this phenomenon.

The modelling results of the additional long wave energy received by the Snow Close ROI from the Rock ROI are summarised in Table 2. Additionally, Table 2 provides the LiDAR differential vertical ablation (*ΔLidar*) for the 3 meteorological periods. *ΔLidar* is calculated based on the trends presented in Table 1, and is the difference between the LiDAR Sen's slope values of the Snow Close ROI and Snow Reference ROI for each period, multiplied by the duration (in days) of the corresponding period.

According to Table 1, the Snow Close ROI ablation is overestimated by the model by 37 cm over the 3 meteorological periods (W.1.P., M.2.P. and W.3.P.; Table 2). As the model does not incorporate snow settlement, the ablation could be potentially even more overestimated. The overestimation suggests part of the energy provided by the boulder was not directly used for snow melt, and may instead be used to warm the snowpack to reach the melting point temperature. Nevertheless, the model finds that the boulder impacts the snow ablation on different magnitudes for each observation period. The 'Wet First Period' is characterized by the lowest ablation, with 10 cm loss, which increase for the 'Mild Second Period' to an additional 17 cm of loss, and finally 13 cm lost during the 'Wet Third Period'. Therefore, the model shows the 'Mild Second Period' leads to an increase in the Snow Close ROI ablation, which also continues after the end of this meteorological period.

5. Discussion

Snowpacks melt at variable rates due to a combination of external factors (such as weather, slope aspect, and shading) and internal factors (such as debris and snow density). From June 12 to June 20, 2022, we conducted high-resolution spatial and temporal observations of the melting snowpack in a subarctic alpine valley of southwestern Yukon, Canada, focusing on surface temperature and elevation changes. Our study examined three specific regions: a reference snow area, a boulder emerging as the snow melts, and the snow adjacent to the boulder. By comparing temperature and elevation differences in these regions, we sought to elucidate the influence of the boulder on snow temperature and melting rates.

During the observation period, weather changes resulted in three distinct subperiods with different meteorological conditions. These weather changes provided a unique opportunity to assess the interplay between weather and snowmelt, particularly how variations in incoming solar radiation and relative humidity affect the boulder and the surrounding snowmelt rates.

Table 2
Comparison between observed "Lidar differential vertical ablation" (ΔLidar) and modelized vertical ablation (ΔLW) on Snow Close ROI.

	Unit	Source	Mean vertical ablation		
			1st period	2nd period	3rd period
ΔLidar	m	Lidar Sen's slopes	+0.00	−0.03	−0.00
ΔLW	m	Model Result	−0.10	−0.17	−0.13

5.1. Heat exchanges and preferential ablation

As detailed in the results section, the three snowpack observation methods used in this study provided valuable insights into the impact of an emerging boulder on snow ablation.

During the clear sky 'Mild Second Period', the TLS results indicate that snow ablation and/or settlement may be enhanced at the Snow Close ROI compared to the Snow Reference ROI. Although the trenching phenomenon was not captured by TLS, these results indicate a potential localized increase in ablation rates near the Snow Close ROI.

Fig. 7a shows a side-view cross-section of the boulder and the adjacent snow throughout the study period. The expected snow profile at the end of the survey (June 20) can be computed: being the snow surface profile measured by photogrammetry at the beginning (June 12) of the survey offset by the observed average ablation. The Average ablation is assumed equal to the mean snow elevation difference of the Snow Reference ROI during the study period. Fig. 7a allows to compare the expected snow profile with the measured snow surface profile obtained by photogrammetry at the end (June 20) of the survey. The comparison between the expected profile without the boulder effect with the measured snow surface profile at the end of the survey reveals a mismatch between the two curves. The area between these profiles represents the influence of the boulder on snow ablation and settlement. The expected and observed snow profiles converge approximately 2 m from the boulder, indicating that the boulder's influence during the survey period was limited to this distance. Additionally, the observed profile at the end of the survey reveals a slope break 24 cm from the boulder, suggesting that multiple processes may contribute to the boulder's effect on snow ablation at different ranges.

TIR images collected at high frequency demonstrate that short-wave radiation can raise the boulder's surface temperature to levels up to 20 °C higher than the ambient air temperature on mild, clear days. The same images show that the surface of the snow in direct contact with the boulder becomes gradually warmer than the snow surface further away. During the 'Wet First Period', the temperatures of all three ROIs were colder, less variable, and more homogeneous compared to during the 'Mild Second Period' (Fig. 6). Additionally, during the 'Mild Second Period', characterized by higher air temperature and less cloud coverage, the temperature of the Snow Close ROI starts to differentiate from that of the Snow Reference ROI, with higher temperatures and increasing heterogeneity. These observations suggest that the Rock ROI may have increased the melting of the proximal part of the Snow Close ROI. Overall, the anomalies in snow surface temperatures and topography observed near the boulder were more intense during the 'Mild Second Period', indicating that meteorological conditions affect both the distance and amplitude of the boulder's impact on the surrounding snow. The results suggest that during warm and sunny weather, boulders already emerging from the snow will amplify the melting of the snow cover in its vicinity.

Figs. 7b–d illustrate the side-view cross-section of the boulder, the observed adjacent snow profile, and the modeled snow profile for the three meteorological periods. Although the use of a 2D model considering only short waves and longwave have proven to be satisfactory to estimate the additional ablation induced by tree trunk on a surrounding subarctic snowpack (Woo and Giesbrecht, 2000), the present model generally overestimates the ablation for the Snow Close ROI (Table 2). Fig. 7b shows strong agreement between the modeled and observed profiles at the end of the 'Wet First Period', with only the proximal portion being overestimated. This suggests that during the 'Wet First Period', the boulder's longwave emissions could explain the snow ablation pattern. In contrast, at the end of the 'Mild Second Period', the model overestimates ablation near the boulder while underestimating it

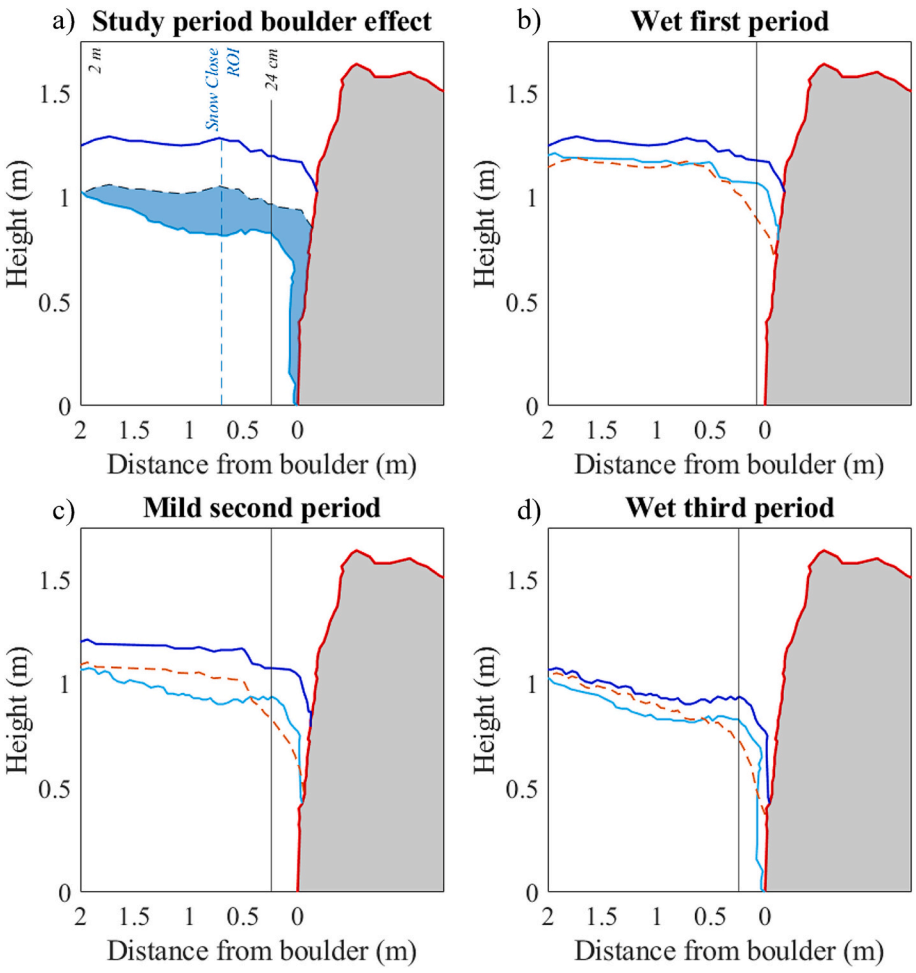

Fig. 7. a) Side view cross-section of the boulder and adjacent snow for the whole study period. The boulder and snow profiles extracted from photogrammetry on June 20 are presented in red and cyan respectively. The snow profile extracted from photogrammetry at the beginning on June 12 is presented in dark blue. The dashed black line represents the expected snow profile at the end of the survey (June 20), assuming the boulder would not affect the snow ablation. The area in blue marks the difference between the expected snow profile (dashed black line) and the observed snow profile (cyan line) at the end of the survey (June 20). The Snow Close ROI maximal extent is represented by a vertical dashed line. The point of convergence of the expected snow profile (dashed black line) and the observed snow profile (cyan line) at the end on June 20 is marked at 2 m and the slope break of the observed snow profile (cyan line) at the end of the survey (June 20) is marked by a vertical black line 24 cm from the boulder curve lowest point. b-d) Depicts the side view section of the boulder and adjacent snow for the 'Wet First Period', the 'Mild Second Period' and the 'Wet Third Period', respectively. For each panel, the boulder on June 20 is presented in red. The snow profile extracted from photogrammetry is represented by a dark blue line and a cyan line for the beginning and end of the meteorological period, respectively. The modelized snow profile at the end of each period is presented as a dashed orange line. The slope break of the observed snow profile (cyan line) at the end of the meteorological period is marked by vertical black lines. (For interpretation of the references to colour in this figure legend, the reader is referred to the web version of this article.)

in the distal regions. This suggests that longwave emissions alone cannot account for the boulder's effect during this period. Finally, at the end of the 'Wet Third Period', the modeled profile fails to align with observations. While the distal regions appear only slightly offset, ablation closer to the boulder significantly deviates from the observed profile, further suggesting additional processes beyond longwave emissions influence the boulder effect.

According to the TIR results, the rock mass may have accumulate heat during the 'Mild Second Period' and its subsequently released it during the 'Wet Third Period'. Suggesting the emerging boulder increases the surrounding energy inputs to the snow, not only through longwave emission but also by storing heat and transferring it to the surrounding snow.

Photogrammetry-derived snow surface profiles next to the boulder (Fig. 5) are in good accordance with the observed position of the slope breaks presented in Fig. 7b–d. The trench width evolution confirms that heat transfer is not limited to radiative effects, as the ablation profile is almost vertical in the trench that forms over time. A purely radiative redistribution of solar radiation would create an ablation pattern dictated by the emitting surface's field of view (Aubry-Wake et al., 2018). In addition, the trench's continuous enlargement even after the 'Second Mild Period' supports the hypothesis that the boulder stores and later redistributes heat captured by modifying the local energy budget.

We observe that the simultaneous interpretation of results from the different methods confirms that emerging boulders redistribute heat during the snow ablation period. Therefore, emerging boulders can significantly modify the ablation pattern of a subarctic snowpack in its vicinity compared to areas without boulders. The boulder effect observed in the area more distal to the boulder indicates that the boulder heat redistribution involves other processes than direct radiative heat exchanges like the local advective fluxes, as suggested by Essery et al. (2006). The formation of trenches observed at the snowpack-boulder interface during this study could not be explained by the model considering long waves only. We anticipate advective fluxes and thermal conduction as being among the heat exchange processes involved the trench formation and growth. Additionally, this ablation pattern may be influenced by snow erosion from meltwater flowing over the surface of the boulder, with the trench potentially channeling both rainfall and

meltwater, thereby accelerating its deepening. Alternatively, the pattern could result from a local anomaly in snow density or changes in snow properties near the boulder.

5.2. Methodology discussion

In addition to understanding snowmelt processes, our research uses a unique combination of observational tools for continuous snowpack monitoring. The following section discusses the lessons learned from utilizing these observation tools.

5.2.1. TIR correction

Our research finds technical considerations for the TIR correction method of Aubry-Wake et al. (2015), a method developed for periglacial environments. The initial step in TIR data correction involves converting the measured temperature to radiance using Planck's law (Vollmer and Möllmann, 2017), followed by partitioning the measured radiance to account for atmospheric absorption and reflected radiance loss. Given that the camera's distance to the areas of interest in our study is approximately 40 m and the air temperature and humidity near the camera and the ROIs are similar, atmospheric transmissivity is nearly equal to 1 for the study period. Additionally, the emissivity of rock and snow are 0.9 and 0.98 respectively (Hori et al., 2006; Rivard et al., 1995), rendering atmospheric radiance absorption and surface reflection almost negligible. Consequently, the primary correction of the TIR data in our study has been due to the CPs offset, indicating that under similar conditions, using only three CPs for correction and maintaining other sensors as validation points may suffice. This simpler calibration approach requires less processing and is feasible without knowledge of the thermal camera sensor wavelengths.

5.2.2. LiDAR measurements of the snowpack ablation

As noted in the results section, the LiDAR measurements of surface elevation of the two snow ROIs exhibit a diurnal pattern, with a slight elevation rise during the night and a decrease during the day, particularly during the 'Mild Second Period'. In addition, this pattern is not observed in the Rock ROI measurements, indicating that the LiDAR equipment is functioning properly. This phenomenon suggests that the LiDAR measurements are sensitive to changes in snow surface properties. According to Deems et al. (2013), the interaction of snow grain size and liquid water content with laser beams may result in uncertainties in snow depth measurement. These anomalous patterns were mainly observable when the snow surface temperature oscillated close to the melting point, i.e., during the 'Mild Second Period' and the 'Wet Third Period'. Therefore, we interpret these patterns primarily as due to diurnal variations in the snow surface liquid water content (i.e., melting and freezing). However, they may also be influenced by indirect near-infrared sunlight reflected off the snow surface, as surface conditions affect snowpacks' optical properties. The findings underscore the need for caution when measuring snow depth with LiDAR, particularly regarding timing, as errors can vary both spatially and temporally. Stationary control points and further analysis of measurements timing impacts are recommended. In addition, drone-based LiDAR may face additional uncertainties due to changing sun angles during flights.

6. Conclusions

A combination of snow surface temperature monitoring using TIR and snow surface topography observation with photogrammetry and TLS was used on a subarctic alpine snowpack in northwest Yukon (Canada) during the melting period of June 2022. This multi-method approach provides valuable insights into the heat redistribution effect caused by emerging boulders during the snow ablation period. The findings indicate that this boulder effect is large enough to modify the ablation pattern on the snowpack surface in close contact with boulders compared to areas without boulders. Additionally, the extent of the boulder influence on the snow ablation and the ablation rate have been shown to be dependent of the meteorological condition and the snowpack conditions.

While the method did not allow us to quantify to which extent each specific component of the snow energy budget was involved in the boulder effect, further efforts in this research area are recommended. In addition, the observations and model results discussed here are from an individual site with specific characteristics. Futures studies should consider multiple boulders-snowpack interactions with diverse characteristics and climatic conditions to assess the general validity of our results. Such efforts could improve the understanding of the physical processes involved. We anticipate that this assessment of the impact of boulders on the snow energy budget will help enhance physically based snow models by integrating the processes involved in heat redistribution in mountain catchments.

Although the boulder effect mainly manifests at a meter-scale in the vicinity of a boulder, its cumulative impact across a landscape could significantly alter snowmelt timing, especially in mountainous regions with dense boulder fields. Understanding these localized heat redistribution effects is essential for refining snowmelt models, particularly in subarctic and alpine regions where accurate predictions of snowpack behaviour are crucial for water management. This study represents the first identification of the boulder effect in a subarctic mountain environment, underscoring the need to incorporate this process into future research and modelling efforts.

CRediT authorship contribution statement

Eole Valence: Writing – original draft, Methodology, Investigation, Formal analysis. **Bastien Charonnat:** Writing – review & editing, Writing – original draft, Formal analysis. **Michel Baraër:** Writing – review & editing, Funding acquisition, Conceptualization. **Kaiyuan Wang:** Writing – review & editing, Formal analysis. **Jeffrey M. McKenzie:** Writing – review & editing, Funding acquisition.

Declaration of competing interest

The authors declare the following financial interests/personal relationships which may be considered as potential competing interests.

Michel Baraer reports financial support was provided by Natural Sciences and Engineering Research Council of Canada. Michel Baraer reports financial support was provided by Natural Resources Canada-Polar Continental Shelf Program. Michel Baraer reports financial support was provided by Research Centre on the Dynamics of the Earth System (GEOTOP). If there are other authors, they declare that they have no known competing financial interests or personal relationships that could have appeared to influence the work reported in this paper.

Acknowledgements

We express our gratitude to the Kluane First Nation and White River First Nation for allowing us to conduct research on their lands and we acknowledge their deep history and relationship with it. We also extend our thanks to the Arctic Institute of North America and the University of Calgary for providing services and access to their facilities at the Kluane Lake Research Station. Additionally, we thank Parks Canada for granting us permission to conduct research in Kluane National Park and Reserve.

The research is supported by the Natural Sciences and Engineering Research Council of Canada, Global Water Futures, the Geotop Research Centre in Earth System Dynamics, Natural Resources Canada's Polar Continental Shelf Program, and McGill University.

Appendix A. Supplementary data

Supplementary data to this article can be found online at https://doi.org/10.1016/j.coldregions.2025.104534.

Data availability

The data are available in Valence and Baraer, 2025, on Borealis dataverse (https://doi.org/10.5683/SP3/NEXJU8).

References

Aubry-Wake, C., Baraer, M., McKenzie, J.M., Mark, B.G., Wigmore, O., Hellström, R.Å., Lautz, L., Somers, L., 2015. Measuring glacier surface temperatures with ground-based thermal infrared imaging. Geophys. Res. Lett. 42 (20), 8489–8497. https://doi.org/10.1002/2015GL065321.

Aubry-Wake, C., Zéphir, D., Baraer, M., McKenzie, J.M., Mark, B.G., 2018. Importance of longwave emissions from adjacent terrain on patterns of tropical glacier melt and recession. J. Glaciol. 64 (243), 49–60. https://doi.org/10.1017/jog.2017.85.

Baker, E.A., Lautz, L.K., McKenzie, J.M., Aubry-Wake, C., 2019. Improving the accuracy of time-lapse thermal infrared imaging for hydrologic applications. J. Hydrol. 571, 60–70. https://doi.org/10.1016/j.jhydrol.2019.01.053.

Bartelt, P., Lehning, M., 2002. A physical SNOWPACK model for the Swiss avalanche warning. Cold Reg. Sci. Technol. 35 (3), 123–145. https://doi.org/10.1016/S0165-232X(02)00074-5.

Bevan, J.M., Kendall, M.G., 1971. Rank Correlation Methods. *The*. Statistician 20 (3), 74. https://doi.org/10.2307/2986801.

Brun, E., Martin, E., Simon, V., Gendre, C., Coleou, C., 1989. An Energy and Mass Model of Snow Cover Suitable for Operational Avalanche forecasting. J. Glaciol. 35 (121), 333–342. https://doi.org/10.3189/S0022143000009254.

Chesnokova, A., Baraër, M., Laperrière-Robillard, T., Huh, K., 2020. Linking Mountain Glacier Retreat and Hydrological changes in Southwestern Yukon. Water Resour. Res. 56 (1), e2019WR025706. https://doi.org/10.1029/2019WR025706.

Clemens-Sewall, D., Polashenski, C., Raphael, I.A., Parno, M., Perovich, D., Itkin, P., Jaggi, M., Jutila, A., Macfarlane, A.R., Matero, I.S.O., Oggier, M., Visser, R.J.W., Wagner, D.N., 2024. High-resolution repeat topography of drifting ice floes in the Arctic Ocean from terrestrial laser scanning. Scientific Data 11 (1), 70. https://doi.org/10.1038/s41597-023-02882-w.

Croux, C., Dehon, C., 2010. Influence functions of the Spearman and Kendall correlation measures. Statis. Meth. & Applicat. 19 (4), 497–515. https://doi.org/10.1007/s10260-010-0142-z.

Deems, J.S., Painter, T.H., Finnegan, D.C., 2013. Lidar measurement of snow depth: a review. J. Glaciol. 59 (215), 467–479. https://doi.org/10.3189/2013JoG12J154.

Dierauer, J.R., Allen, D.M., Whitfield, P.H., 2021. Climate change impacts on snow and streamflow drought regimes in four ecoregions of British Columbia. Canadian Water Res. J. / Revue Canadienne Des Ressources Hydriques 46 (4), 168–193. https://doi.org/10.1080/07011784.2021.1960894.

Essery, R., Granger, R., Pomeroy, J., 2006. Boundary-layer growth and advection of heat over snow and soil patches: Modelling and parameterization. Hydrol. Process. 20 (4), 953–967. https://doi.org/10.1002/hyp.6122.

Evin, M., Fabre, D., Johnson, P.G., 1997. Electrical Resistivity Measurements on the Rock Glaciers of Grizzly Creek, St Elias Mountains, Yukon. Permafr. Periglac. Process. 8 (2), 179–189. https://doi.org/10.1002/(SICI)1099-1530(199732)8:2<179::AID-PPP247>3.0.CO;2-C.

Gergely, M., Schneebeli, M., Roth, K., 2010. First experiments to determine snow density from diffuse near-infrared transmittance. Cold Reg. Sci. Technol. 64 (2), 81–86. https://doi.org/10.1016/j.coldregions.2010.06.005.

Gray, J., Morland, L.W., Colbeck, S.C., 1995. The effect of change in thermal properties on the propagation of a periodic thermal wave: Application to a snow-buried rocky outcrop. J. Geophys. Res. Solid Earth 100 (B8), 15267–15279.

Grünewald, T., Schirmer, M., Mott, R., Lehning, M., 2010. Spatial and temporal variability of snow depth and ablation rates in a small mountain catchment. Cryosphere 4 (2), 215–225. https://doi.org/10.5194/tc-4-215-2010.

Hamed, K.H., 2009. Exact distribution of the Mann–Kendall trend test statistic for persistent data. J. Hydrol. 365 (1–2), 86–94. https://doi.org/10.1016/j.jhydrol.2008.11.024.

Hannula, H.-R., Pulliainen, J., 2019. Spectral reflectance behavior of different boreal snow types. J. Glaciol. 65 (254), 926–939. https://doi.org/10.1017/jog.2019.68.

Hori, M., Aoki, T., Tanikawa, T., Motoyoshi, H., Hachikubo, A., Sugiura, K., Yasunari, T. J., Eide, H., Storvold, R., Nakajima, Y., Takahashi, F., 2006. In-situ measured spectral directional emissivity of snow and ice in the 8–14 μm atmospheric window. Remote Sens. Environ. 100 (4), 486–502. https://doi.org/10.1016/j.rse.2005.11.001.

Johnson, P.G., 1978. Rock glacier types and their drainage systems, Grizzly Creek, Yukon Territory. Can. J. Earth Sci. 15 (9), 1496–1507. https://doi.org/10.1139/e78-155.

Jordan, R.E., 1991. A One-dimensional temperature model for a snow cover: Technical documentation for SNTHERM, 89.

Kinar, N.J., Pomeroy, J.W., 2015. Measurement of the physical properties of the snowpack. Rev. Geophys. 53 (2), 481–544. https://doi.org/10.1002/2015RG000481.

Markstrom, S., Hay, L., Ward-Garrison, C., Risley, J., Battaglin, W., Bjerklie, D., Chase, K., Christiansen, D., Dudley, R., Hunt, R., 2011. Integrated Watershed-Scale Response to climate Change for selected Basins across the United States. US Geol. Surv. Sci. Investig. Rep. 2011, 143.

Marsh, P., Pomeroy, J.W., 1996. Meltwater fluxes at an Arctic forest-tundra site. Hydrol. Process. 10 (10), 1383–1400. https://doi.org/10.1002/(SICI)1099-1085(199610)10:10<1383::AID-HYP468>3.0.CO;2-W.

Mas, A., Baraer, M., Arsenault, R., Poulin, A., Préfontaine, J., 2018. Targeting high robustness in snowpack modeling for Nordic hydrological applications in limited data conditions. J. Hydrol. 564, 1008–1021. https://doi.org/10.1016/j.jhydrol.2018.07.071.

Mellor, M., 1977. Engineering Properties of Snow. J. Glaciol. 19 (81), 15–66. https://doi.org/10.3189/S002214300002921X.

Mott, R., Egli, L., Grünewald, T., Dawes, N., Manes, C., Bavay, M., Lehning, M., 2011. Micrometeorological processes driving snow ablation in an Alpine catchment. Cryosphere 5 (4), 1083–1098. https://doi.org/10.5194/tc-5-1083-2011.

Mountain Research Initiative EDW Working Group, 2015. Elevation-dependent warming in mountain regions of the world. Nat. Clim. Chang. 5 (5), 424–430. https://doi.org/10.1038/nclimate2563.

Notarnicola, C., 2022. Overall negative trends for snow cover extent and duration in global mountain regions over 1982–2020. Sci. Rep. 12 (1), 13731. https://doi.org/10.1038/s41598-022-16743-w.

Paquotte, A., Baraer, M., 2022. Hydrological behaviour of an ice-layered snowpack in a non-mountainous environment. Hydrol. Process. 36 (1), e14433. https://doi.org/10.1002/hyp.14433.

Pomeroy, J.W., Brun, E., 2001. Physical properties of snow. Snow Ecology: An Interdisciplinary. Examinat. Snow-Covered Ecosyst. 45, 118.

Rantanen, M., Karpechko, A.Yu., Lipponen, A., Nordling, K., Hyvärinen, O., Ruosteenoja, K., Vihma, T., Laaksonen, A., 2022. The Arctic has warmed nearly four times faster than the globe since 1979. Communicat. Earth & Environ. 3 (1), 168. https://doi.org/10.1038/s43247-022-00498-3.

Rivard, B., Thomas, P.J., Giroux, J., 1995. Precise emissivity of rock samples. Remote Sens. Environ. 54 (2), 152–160. https://doi.org/10.1016/0034-4257(95)00130-S.

Robledano, A., Picard, G., Arnaud, L., Larue, F., Ollivier, I., 2022. Modelling surface temperature and radiation budget of snow-covered complex terrain. Cryosphere 16 (2), 559–579. https://doi.org/10.5194/tc-16-559-2022.

Rutter, N., Cline, D., Li, L., 2008. Evaluation of the NOHRSC Snow Model (NSM) in a One-Dimensional Mode. J. Hydrometeorol. 9 (4), 695–711. https://doi.org/10.1175/2008JHM861.1.

Sen, P.K., 1968. Estimates of the Regression Coefficient based on Kendall's Tau. J. Am. Stat. Assoc. 63 (324), 1379–1389. https://doi.org/10.1080/01621459.1968.10480934.

Shu, S., Yu, O.-Y., Schoonover, C., Liu, H., Yang, B., 2023. Unmanned Aerial Vehicle-Based Structure from Motion Technique for Precise Snow Depth Retrieval—Implication for Optimal Ground Control Point Deployment Strategy. Remote Sensing 15 (9), 2297. https://doi.org/10.3390/rs15092297.

Sun, F., Berg, N., Hall, A., Schwartz, M., Walton, D., 2019. Understanding End-of-Century Snowpack Changes Over California's Sierra Nevada. Geophysical Research Letters 46 (2), 933–943. https://doi.org/10.1029/2018GL08036.

Tjoelker, A.R., Baraër, M., Valence, E., Charonnat, B., Masse-Dufresne, J., Mark, B.G., McKenzie, J.M., 2024. Drone-based Ground-Penetrating Radar with Manual Transects for improved Field surveys of buried Ice. Remote Sens. 16 (13), 13. https://doi.org/10.3390/rs16132461.

Turcotte, R., Fortin, L.-G., Fortin, V., Fortin, J.-P., Villeneuve, J.-P., 2007. Operational analysis of the spatial distribution and the temporal evolution of the snowpack water equivalent in southern Québec, Canada. Hydrol. Res. 38 (3), 211–234. https://doi.org/10.2166/nh.2007.009.

Valence, E., Baraer, M., Rosa, E., Barbecot, F., Monty, C., 2022. Drone-based ground-penetrating radar (GPR) application to snow hydrology. Cryosphere 16 (9), 3843–3860. https://doi.org/10.5194/tc-16-3843-2022.

Vollmer, M., Möllmann, K., 2017. Infrared Thermal Imaging: Fundamentals, Research and Applications, 1st ed. Wiley. https://doi.org/10.1002/9783527693306.

Warren, M.E., 2019. Automotive LIDAR Technology. Sympos. VLSI Circuits 2019, C254–C255. https://doi.org/10.23919/VLSIC.2019.8777993.

Wetlaufer, K., Hendrikx, J., Marshall, L., 2016. Spatial Heterogeneity of Snow Density and its Influence on Snow Water Equivalence estimates in a large Mountainous Basin. Hydrology 3 (1), 3. https://doi.org/10.3390/hydrology3010003.

Woo, M., Giesbrecht, M.A., 2000. Simulation of snowmelt in a subarctic spruce woodland: 1. Tree model. Water Resour. Res. 36 (8), 2275–2285. https://doi.org/10.1029/2000WR900094.